Spectral observations of FUV auroral arcs and comparison with inverted-V precipitating electrons

C. N. Lee,[1] K. W. Min,[1] J.-J. Lee,[2] G. K. Parks,[3] M. O. Fillingim,[3] D. Lummerzheim,[4] K. S. Cho,[2] K.-H. Kim,[5] Y. H. Kim,[6] Y. D. Park,[2] W. Han,[2] J. Edelstein,[3] and E. Korpela[3]

Received 25 November 2009; revised 16 April 2010; accepted 21 May 2010; published 28 September 2010.

[1] This paper presents first simultaneous observations of far ultraviolet (FUV) spectra of discrete and diffuse auroras, together with precipitating electrons measured on the same spacecraft, to emphasize the importance of high-resolution FUV images for accurate estimation of precipitating energy flux in the auroral region. An FUV spectrograph image with ~2 km × 3 km resolution show small-scale features were embedded in the auroral arcs. Comparison of peak energies of inverted-V events with the corresponding FUV spectra shows that the observed long band N_2 Lyman-Birge-Hopfield (LBH) emission (long LBH band (LBHL): 160.0–171.5 nm) varied more sensitively to the peak energies compared to the short band. Comparison of the inverted-V structures and their energy fluxes with the LBHL irradiance for ~10 km × 10 km regions show they are well correlated for peak energy >2 keV. When the data are averaged over a larger area (70 km × ~140 km), on the other hand, the LBHL irradiance becomes less bright for the corresponding electron energy flux due to the contribution from the low-intensity background diffuse aurora produced by secondary electrons. This study demonstrates a reliable relationship between precipitating electron energy flux and LBHL intensity is obtained only if the precipitating region and FUV intensity are locally matched with a scale of less than 10 km corresponding to the size of discrete auroras.

Citation: Lee, C. N., et al. (2010), Spectral observations of FUV auroral arcs and comparison with inverted-V precipitating electrons, *J. Geophys. Res.*, *115*, A09223, doi:10.1029/2009JA015071.

1. Introduction

[2] Auroral emission is produced by collisions of energetic particles with atmospheric neutral particles and ions. Especially, it is known that N_2 far ultraviolet (FUV) aurora is generated at altitudes of 80~120 km by the precipitating electrons of 1~15 keV [*Germany et al.*, 2001; *Frey et al.*, 2003]. The auroral intensities and spectra strongly depend on the energy flux as well as the characteristic energy of the precipitating particles [*Strickland et al.*, 1983; *Germany et al.*, 1990, 1994]. For example, the Lyman-Birge-Hopfield (LBH) bands, which result from the electron impact excitation of N_2, suffer from significant absorption by O_2 near 140.0 nm while the absorption is negligible near 170.0 nm. As high-energy particles are able to penetrate more deeply into the atmosphere where the O_2 absorption is significant, the corresponding ratio of the long LBH band (LBHL) intensity over that of the short band (LBHS) is much higher than the ratio for less energetic particles. In this regard, FUV images that have short and long LBH spectral bands can be used to extract information on the precipitating auroral particles [*Torr et al.*, 1995; *Paxton et al.*, 1999; *Frey et al.*, 2003]. For example, 140.0~160.0 nm and 160.0~180.0 nm bands were adopted for LBHS and LBHL observations, respectively, on the Polar spacecraft [*Brittnacher et al.*, 1997].

[3] Auroral emission involves various complicated physical processes such as particle collisions as well as scattering and absorption of the emitted radiation. As satellites have been equipped with instruments that provide FUV images, considerable effort has been made to model these processes for the FUV auroras. One of the difficulties has been observational verification of the relationship between auroral emission and the characteristics of precipitating electrons because these measurements have been made from different spacecraft. For example, the Polar Ultraviolet Imager's (UVI) results were compared with the energy characteristics of incident particles that were obtained from the Defense Meteorological Satellite Program [*Germany et al.*, 1997; *Newell et al.*, 1999; *Liou et al.*, 1999]. The auroral images from the Imagers for Magnetopause-to-Aurora Global

[1]Department of Physics, Korea Advanced Institute of Science and Technology, Daejeon, Korea.
[2]Korea Astronomy and Space Science Institute, Daejeon, Korea.
[3]Space Sciences Laboratory, University of California, Berkeley, California, USA.
[4]Geophysical Institute, University of Alaska Fairbanks, Fairbanks, Alaska, USA.
[5]School of Space Research, KyungHee University, Yongin, Korea.
[6]Astronomy and Space Science, ChungNam National University, Daejeon, Korea.

0148-0227/10/2009JA015071

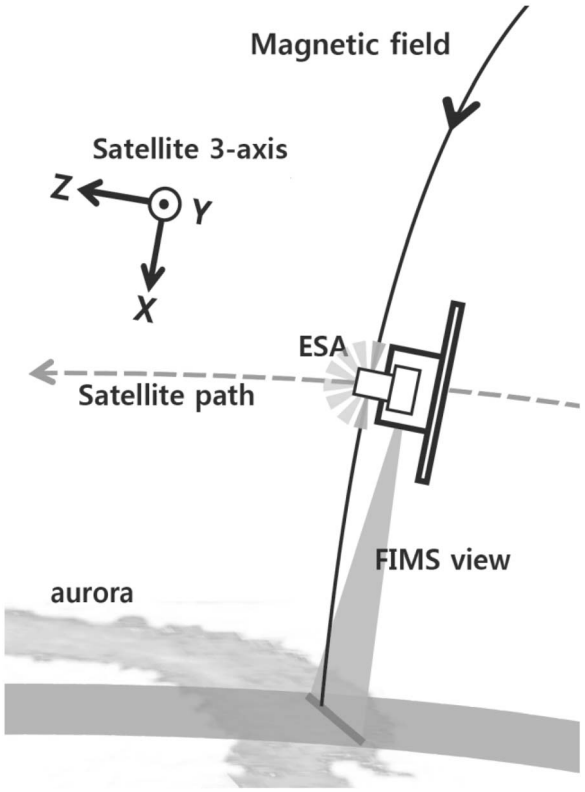

Figure 1. Geometry of STSAT-1 auroral observations. The satellite's attitude is maneuvered so that its x-axis (parallel to the field of view of Far-Ultraviolet Imaging Spectrograph (FIMS)) is aligned along the geomagnetic field line and the z-axis is parallel to the orbital motion of the satellite.

Exploration (IMAGE) satellite were compared with the particle data that were obtained from the Fast Auroral Snapshot (FAST) satellite [*Frey et al.*, 2001; *Gérard et al.*, 2001; *Mende et al.*, 2003] and the NOAA observations [*Coumans et al.*, 2002; *Meurant et al.*, 2003] as well as from the DMSP observations [*Zhang et al.*, 2003].

[4] Moreover, previous FUV observations were carried out from high altitudes, and although they provided good global coverage, the images had spatial resolution much larger than typical auroral structures. For example, Polar spacecraft at an altitude of 9 R_E provided nominal images with 40 × 40 km^2 resolution [*Torr et al.*, 1995; *Brittnacher et al.*, 1997]. The Wideband Imaging Camera on the IMAGE spacecraft from an altitude of 7 R_E obtained images with 100 × 100 km^2 resolution [*Frey et al.*, 2003]. Hence it was difficult to deduce an accurate picture of the actual precipitating particles from these low-resolution images, since both the auroral features, particle fluxes and energies can vary over a scale as small as ~1 km [*Kunitake and Oguti*, 1984; *McFadden et al.*, 1987].

[5] We have compared FUV auroral spectra with the energy spectra of primary precipitating electrons in the energy range from ~100 eV to 20 keV obtained simultaneously from the same spacecraft. Inverted-V events were selected from the electron spectra and their peak energies were compared with the FUV spectra at the footprint of the magnetic field lines. This represents the first opportunity the instruments had sufficient spectral and spatial resolutions to compare the FUV line intensities to the peak energies of inverted-V events.

[6] The results show that the observed long LBH spectra varied more sensitively to the peak energies than the short band spectra, probably because of the stronger absorption for higher peak energies at short wavelengths. We also find good correlation is obtained between the electron energy flux and LBHL irradiance for events that had peak energy >2 keV while those with lower peak energy showed diverse LBHL irradiance for similar energy fluxes. When the data are averaged over an area 70 km × 140 km, good correlation is found again even including the events that had peak energies <2 keV but with significantly lower corresponding LBHL irradiance because of the contributions from backscattered softer secondary atmospheric electrons that form a diffuse region within which discrete auroras corresponding to the inverted-V events exist. The present study demonstrates the importance of utilizing high-resolution FUV images for accurate estimation of precipitating energy flux in the auroral region.

2. Instrumentation

[7] Our observations were made on the first Korean scientific microsatellite, Science and Technology Satellite-1 (STSAT-1) launched on 27 September 2003 into a 685 km circular Sun-synchronous orbit whose equatorial crossing time was at 2200 MLT. The inclination angle was 98.2° and its orbital period was 98.5 min. STSAT-1 is a three-axis stabilized satellite with a star tracker that can provide attitude information with an accuracy of 5′. The satellite operated until May 2005 when it suffered battery failure and the mission was terminated.

[8] The main scientific purpose was to study the FUV radiation that originated from hot gases in our galaxy such as supernova remnants. The primary payload was a Far-Ultraviolet Imaging Spectrograph (FIMS), also known as Spectroscopy of Plasma Evolution from Astrophysical Radiation (SPEAR). FIMS is an imaging spectrograph capable of measuring FUV emission lines from 134.0 to 171.5 nm with a spectral resolution of 0.25–0.3 nm [*Edelstein et al.*, 2006a, 2006b]. The field of view (FOV) is 7.4° × 4.5′ with a 5′ imaging resolution along the slit that corresponds to a swath width of ~76 km with ~1 km spatial resolution at a height of 100 km. It should be noted that photons are recorded at the rate of 10 Hz, corresponding to ~0.7 km resolution at a height of 100 km with the satellite speed of ~7.5 km/s.

[9] FIMS was occasionally used to observe nightside auroras in the nadir direction, as shown in Figure 1. Plasma instruments aboard the spacecraft measured precipitating electrons simultaneously. The satellite's attitude was controlled to within 5° during the auroral observations using magnetometers while the attitude information can be obtained later with less than 0.2° by comparing the measurements of the magnetometers with the reference geomagnetic field. Hence careful comparison is required, including time shifts of a few seconds between the FIMS and plasma measurements that arise from the misalignment of the satellite axis with the geomagnetic field lines, to match the FUV images with the data from the plasma instruments to ensure those in

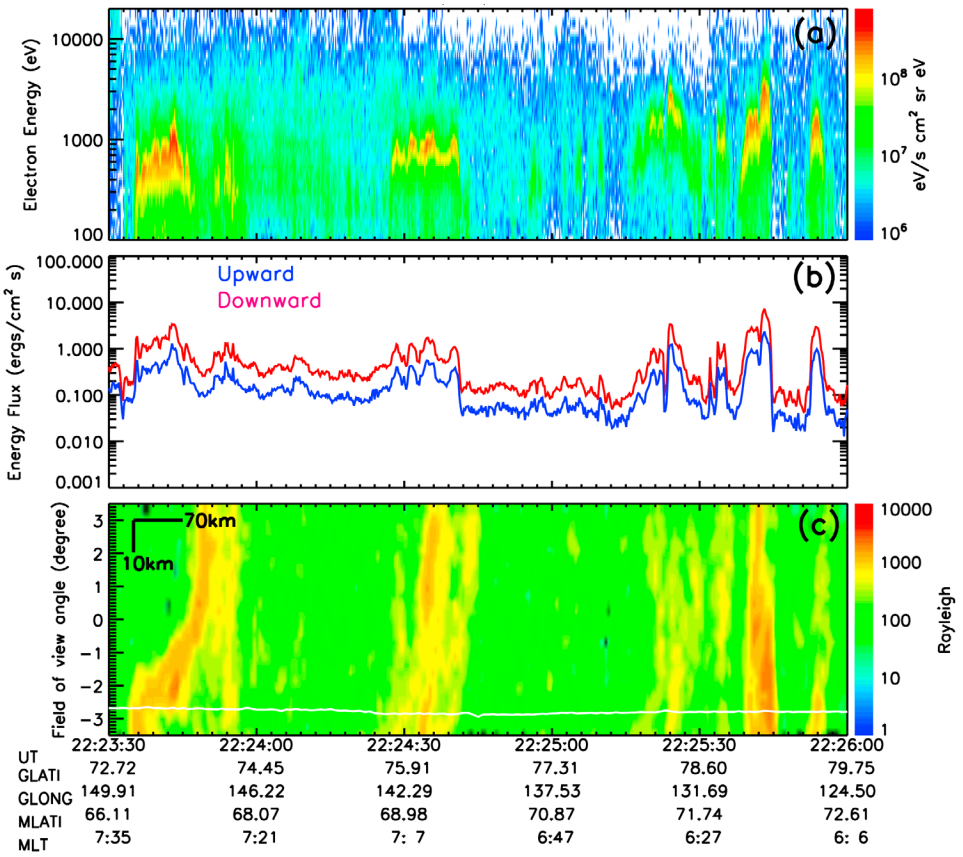

Figure 2. A summary plot that shows a typical FIMS image and the electrostatic analyzer (ESA) precipitating electron fluxes obtained on 2 February 2004. (a) ESA electron energy flux spectrogram from 100 eV to 20 keV, (b) upward (blue) and downward (red) total electron energy flux, and (c) the FIMS FUV auroral image, which is integrated over wavelengths from 134.0 to 171.5 nm with log-scale intensity (Rayleigh). The white line in the FIMS image indicates the footprint on the atmosphere of the geomagnetic field that passes through the instantaneous satellite location at an altitude of 100 km. Shown in the top left corner in Figure 2c are the horizontal and vertical scales of the image.

consideration were truly corresponding events. The FUV auroral observations were complemented by in situ measurements of electrons that used a set of plasma instruments called Space Physics Package (SPP) [*Lee et al.*, 2005]. The SPP consisted of an electrostatic analyzer (ESA), a solid state telescope(SST), a Langmuir probe (LP), and a magnetometer. Of these instruments, the data of ESA were used for the present auroral study.

[10] The ESA is a top hat type electrostatic analyzer design and measures electrons from 100 eV to 20 keV in 30 channels with an energy resolution of ~10%. Since it was installed on a three-axis stabilized satellite, the analyzer provided two-dimensional (2-D) angular information from 0° to 180°, with 22.5° angular resolution. Electrons along and against the direction of the magnetic field were measured when the satellite x-axis was aligned to the geomagnetic field. The SST and LP measured energetic electrons from 170 keV to 360 keV and ambient thermal electrons, respectively. The magnetometer was used to determine the satellite's attitude. The SPP instruments were equipped with fast electronics with a time resolution 200 ms for ESA which corresponded to 1.4 km at a height of 100 km. Both FIMS and SPP were ideal for studying auroral features of ~km size and the characteristics of the precipitating electrons.

3. Auroral Observation

[11] Figure 2a shows an example of the ESA energy flux spectrogram for precipitating electrons around a 0° pitch angle and the FUV auroral image (Figure 2c) obtained on STSAT-1. Figure 2b shows the total energy flux from 100 eV to 20 keV for the electrons moving upward (blue line) and downward (red line) of the geomagnetic field. At the time of these observations on 2 February 2004, the geomagnetic activity was slightly disturbed with Kp = 4.

[12] A remarkable good agreement is observed between the structures of FUV emissions and the total energy flux of the precipitating electrons. In the FUV auroral image, the intensity is given in logarithmic scale with a 2 km (along the track) × 3 km (across the track, i.e., along the slit) bin size. Figure 2c shows discrete aurora arcs embedded in the diffuse background. These discrete arcs correspond to the inverted-V events shown in Figure 2a. The intensity of the diffuse background produced by the secondary electrons is

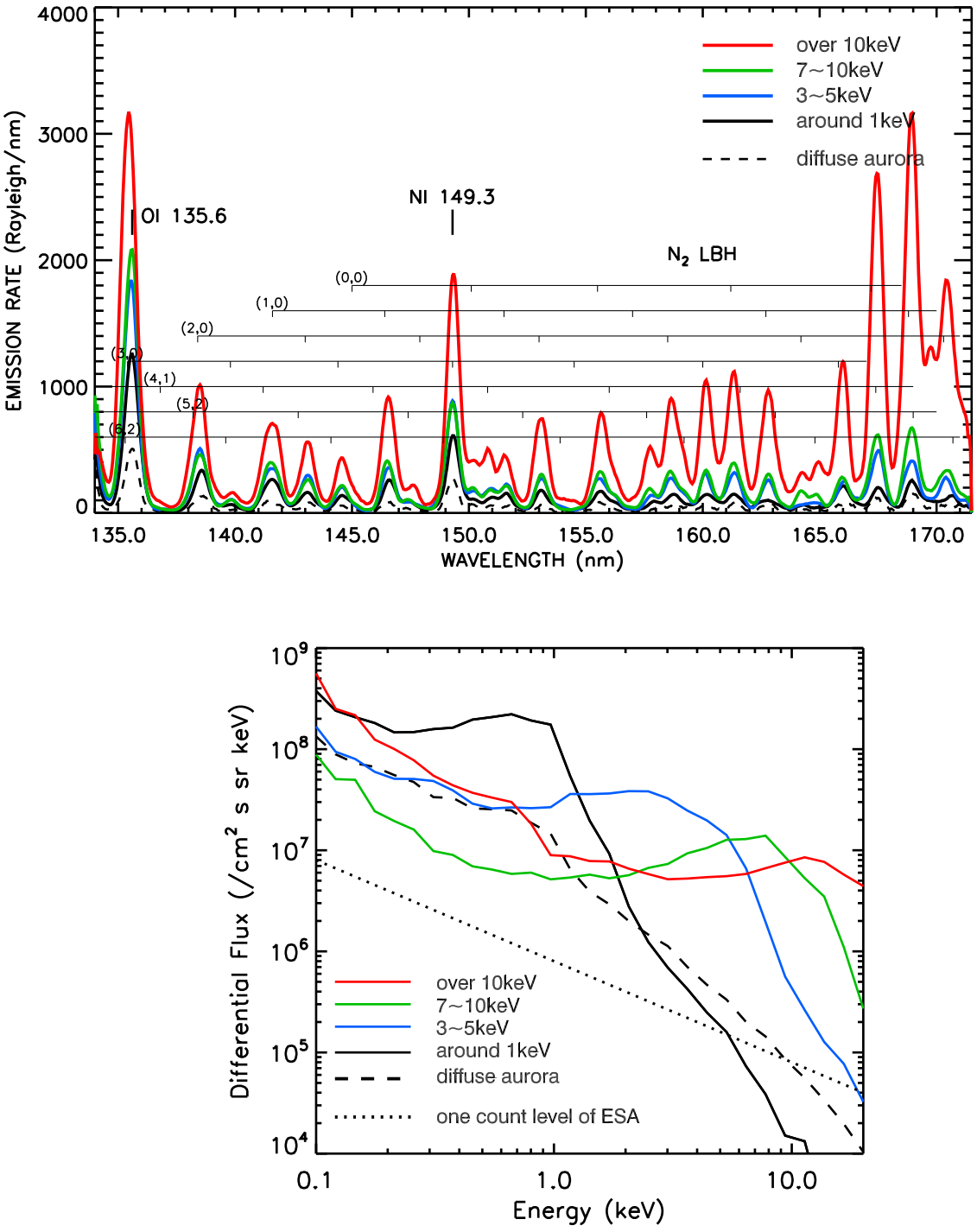

Figure 3. (top) FIMS line spectra plotted for different peak energies of precipitating electrons. The spectrum of the diffuse aurora (dotted line) is also plotted for comparison. (bottom) Differential electron energy spectra for the 0° pitch angle, which corresponds to the FUV spectra shown in Figure 3 (top).

approximately 100 R (Rayleigh). It should be noted that the detector dark background rate is from 0.2 to 0.4 counts/s/nm, which corresponds to ~2 R when integrated over the whole wavelength band. The width of the discrete arcs is around 20 km and is elongated in the east-west direction over the whole FIMS FOV, ~70 km. The peak intensity of the discrete arcs is ~4 kR, higher than ~1 kR for typical aurora arcs associated with 1 keV precipitated electrons [e.g., *Frey et al.*, 2003].

[13] Next, we focus on the variations of the FUV emission line spectrum with the changes in the energies of the precipitating electrons. The inverted-V events for this study were selected during February and October of 2004 when STSAT-1 was observing auroras regularly. The number of

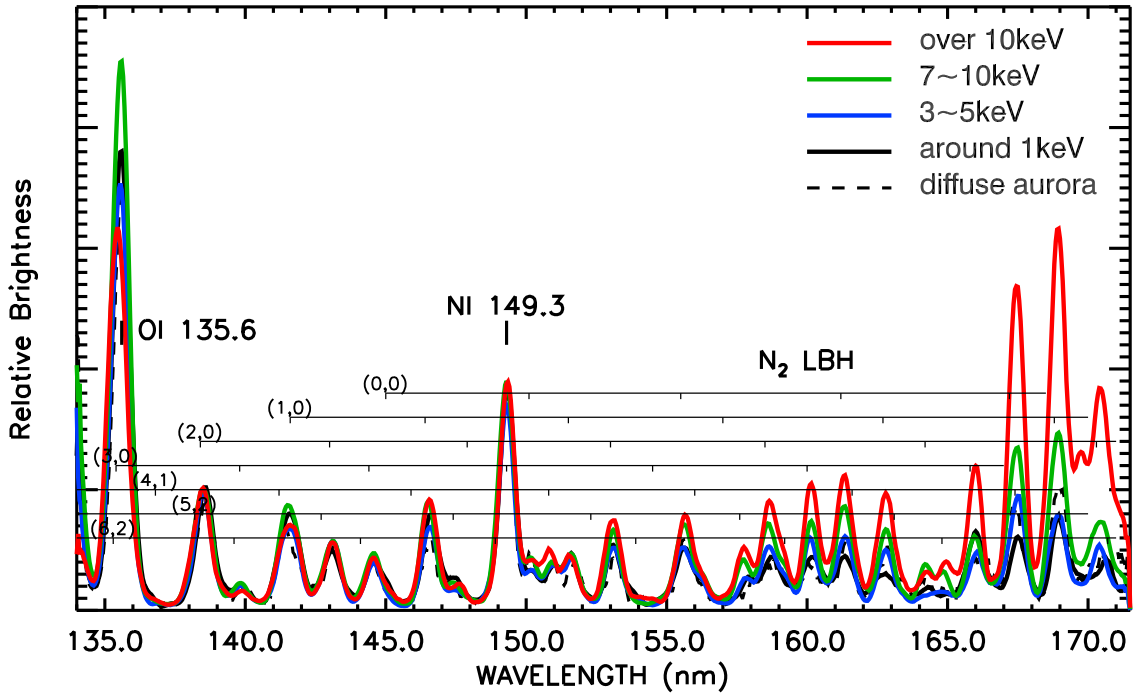

Figure 4. FIMS line spectra normalized to the N_2 138.4 nm intensity, corresponding to Figure 3 (top).

events selected is 49 and they all occurred during rather geomagnetically quiet time with K_p index 0 to 4. The magnetic local time was 0600–800 MLT in the morning sector and and 2300–0100 in the midnight sector. Figure 3 (top) shows the FIMS spectra corresponding to the inverted-V events shown in Figure 3 (bottom) with peak energies at ~1 keV (black), 3–5 keV (blue), 7–10 keV (green), and >10 keV (red). For comparison purposes, the spectrum of the diffuse (dashed) aurora is also included. The emission lines have been identified from the experimental results of *Ajello et al.* [1985].

[14] The differential electron spectra for the pitch angle 0° are shown in Figure 3 (bottom) for the corresponding energy bins of Figure 3 (top). The electron spectra of the inverted-V events in Figure 3 (bottom) show rather broad peaks as they are accumulated spectra of several events. The high-energy part of the 1 keV electron spectrum falls off more rapidly in the case of the present discrete arc than the diffuse aurora. The electron differential spectrum from the diffuse background follows a power law form with the power of ~−1.7.

[15] The line spectra of Figure 3 (top) show that the observed line intensity increases more rapidly with increase in peak energy for wavelengths longer than 155.0 nm. That is likely due to the strong absorption by Schumann-Runge (S-R) O_2 continuum at short LBH bands that occurs at altitudes of 100–200 km [*Carver et al.*, 1978; *Yoshino et al.*, 2005]. However, as the observed line intensity depended on the electron flux as well as the characteristic energy, we have plotted in Figure 4 the same spectra normalized to the intensity at 138.4 nm, where the S-R absorption cross section is maximum within the N_2 LBH band, to examine the energy dependence more clearly. As can be seen in Figure 3, the relative line intensity increases more or less steadily for long wavelengths, especially longer than 160.0 nm while it is almost the same for wavelengths shorter than 150.0 nm. We have estimated the ratios of the LBHL intensities to those of the short band LBH (LBHS: 140.0 nm–150.0 nm). The results are 0.9, 1.1, 1.4, and 2.7 for the peak energies <1 keV, 3–5 keV, 7–10 keV, and >10 keV, respectively.

[16] Examination of Figure 3 (top) in the region around 135.6 nm shows a shift of line center to 135.4 nm for electron energy >10 keV. The shift is probably due to the enhanced contribution from LBH 135.4 nm. However, our instrument does not resolve LBH 135.4 nm from OI 135.6 nm clearly and the exact cause of this shift is not understood at this time.

4. Discussion

[17] A model calculation for the FUV spectrum was performed that involved the observational electron spectra in Figure 3 (bottom). For this calculation, the model of *Lummerzheim and Lilensten* [1994] was utilized which used a multistream approach to calculate the electron intensity as a function of energy and altitude. This code uses a discrete-ordinate method to solve for the energy degradation and electron transport. Volume emissivity is calculated at each grid point, and then radiation transport equation is solved along the line of sight toward the satellite with O_2 absorptions taken into account to obtain intensity. The atmospheric conditions that were needed as input for the simulations were obtained by utilizing the Mass Spectrometer Incoherent Scatter 90 (MSIS-90) model [*Hedin*, 1991], and they were chosen in this study to represent the northern auroral zone in the midnight sector near the equinox. The input *Ap* index was 12 and the input solar *F*10.7 flux was 73.3. These values represent the overall average during the period of observations (February and October 2004).

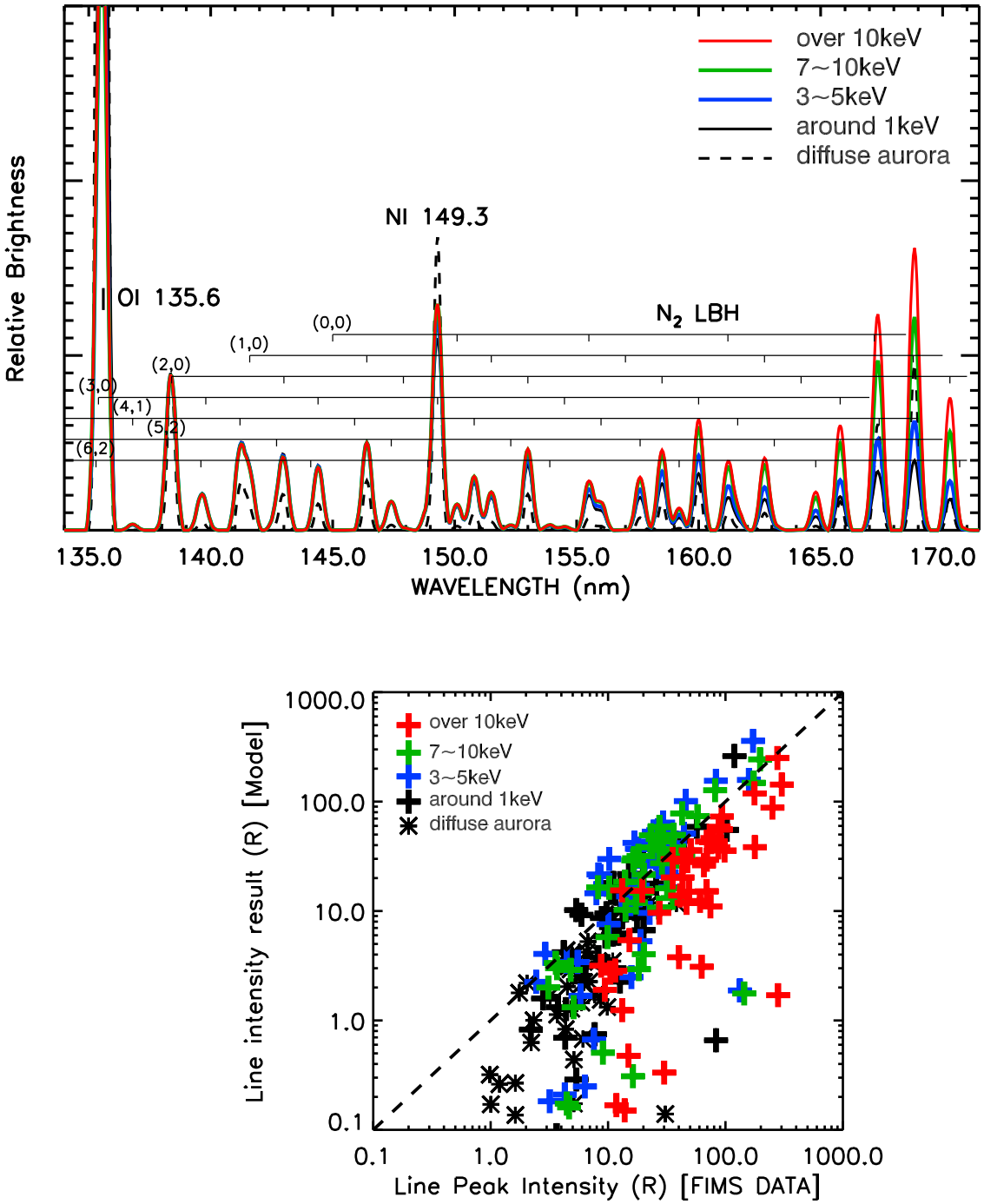

Figure 5. (top) Model FUV spectra obtained for the electron spectra in Figure 3 (bottom) with energy extrapolated to 70 keV. (bottom) Comparison plot between FIMS observation (Figure 3, top) and modeling result (Figure 5 (top)). Peak intensities from two figures are selected. The color symbols denote the peak electron energy levels.

[18] Using the observed fluxes as input, we see the predicted emission line intensities were in general agreement with the observed intensities. The results are shown in Figure 5. Figure 5 (top) is the normalized intensity to the 138.4 nm line for the model results. We have convolved the model results with the FIMS resolution which is 0.3 nm. Figure 5 (bottom) is the comparison plot between the model and the observation, showing the peak intensities of the observation and the model for all the peaks in Figure 5 (top) between 134.0 nm and 171.5 nm of the FIMS wavelength interval. While the model spectra look remarkably similar to the observed spectra, the dependence of the LBHL intensity on the peak energy is less significant in the model spectra compared to the observed spectra. In addition, the model intensity of OI 135.6 nm seems to be much higher than the observed intensity. Though extrapolation of the electron spectra to 70 keV resulted in better agreement in that the intensity ratio of LBHL to LBHS has improved from 1.3 to

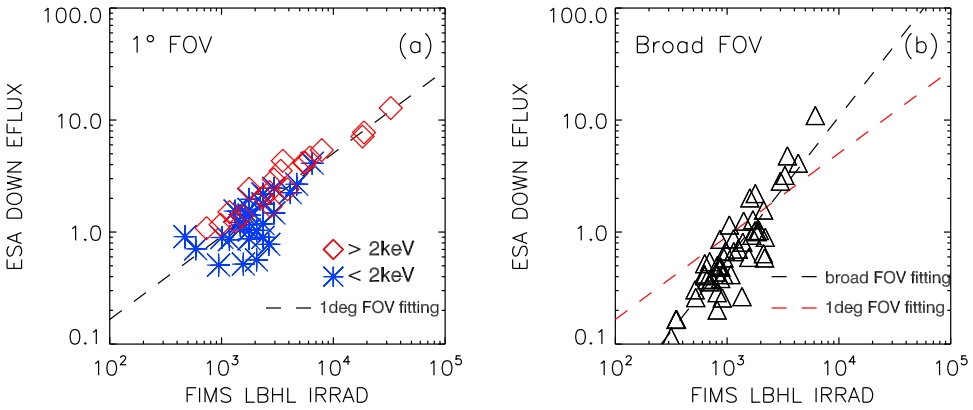

Figure 6. Correlation between the FIMS long Lyman-Birge-Hopfield band irradiance (Rayleighs) and the downward ESA electron energy flux (ergs/cm^2/s) (a) for a bin size of ~10 km × 10 km. The blue asterisks correspond to the inverted-V events with a peak energy <2 keV and the red diamonds to >2 keV), and (b) for the data averaged over 70 km × 140 km. The red dotted line in Figure 6b represents fitting results from Figure 6a.

1.7 for the peak energy >10 keV, for example, these discrepancies may still come from the uncertainty in the electron spectrum. Uncertainty in the photoionization cross sections, especially for high-energy electrons, is also another possibility.

[19] As mentioned earlier, in situ particle observations on board the satellite provide information on the energy and flux of precipitating particles only locally. However, satellite images can provide global pictures of the whole auroral region. Therefore some efforts have been made to obtain reliable estimations of precipitating energy flux from FUV images. *Carbary et al.* [2004] for example compared data from UVI on the Polar satellite obtained for the LBHL passband 160.0–180.0 nm with precipitating particle measured by the DMSP F12 and F13 satellites. They found good correlations between the electron energy flux and photon irradiance for the premidnight and dawn sectors when the dayglow effects were minimal. The spatial resolution was ~110 km, that corresponded to 1° latitudinal bin.

[20] We performed a similar analysis using simultaneously obtained ESA and FIMS data. Forty nine inverted-V events that occurred during the months of February and October of 2004 were selected. The data were averaged with 1° FOV bins, corresponding to 10 km at an altitude of 100 km. The events were divided into two groups, one with peak energy >2 keV and the other with peak energy <2 keV. The downward energy flux was plotted against the corresponding FIMS LBHL irradiance obtained for the wavelength range 160.0–171.5 nm (Figure 6a). The data were also averaged over a larger region that contained the inverted-V events, ~70 km (entire FIMS FOV) × 140 km (20 s data across the track), which was similar to the resolution used by *Carbary et al.* [2004]. The results are shown in Figure 6b. Note that our data came mostly from the morning and midnight sectors.

[21] The correlation between the energy flux and the LBHL irradiance is quite good for the events in Figure 6a. Fitting the data with a simple power law $I(x) = Ax^P$, where I is the downward energy flux in ergs/cm^2/s and x is the LBHL irradiance in Rayleighs, the spectral index $P = 0.65$ is revealed with a correlation coefficient of 0.96 for >2 keV (red diamonds). The inverted-V events that had a peak energy <2 keV (blue asterisks) are scattered over a wide range of LBHL irradiance for small energy fluxes. Lower-energy electrons with larger impact cross sections suffer more scattering during their transit to the region of LBHL emission where the atmosphere is rich with molecular nitrogen. In contrast, higher-energy electrons can penetrate to this altitude effectively and produce LBHL emission that is more or less proportional to the precipitating electron energy flux.

[22] When the data are averaged over a large area (Figure 6b), the correlation between the energy flux and the LBHL irradiance is also good with a correlation coefficient of 0.90 even with inclusion of cases that had peak energies <2 keV. However, the spectral index becomes $P = 1.28$, which is similar to the value of $P = 1.23$ obtained by *Carbary et al.* [2004] for observations in the premidnight regions. The difference of the low-resolution case, in which the data are averaged over a wide region can be interpreted as originating from the contribution of the diffuse component of the auroras that are associated with the low-level flux of precipitating electrons with power law spectra that do not have peak energies.

[23] When the intense discrete arcs that are generally produced by high-energy electrons are integrated with the diffuse background, the resulting intensity is lowered, as can be seen in Figure 6. The red diamonds located above 10 kR at the high end of the electron energy flux in Figure 6a are shifted to below 10 kR in Figure 6b as the bin size increases by a factor of ~10. The corresponding change in the energy flux does not seem to be that significant. On the other hand, LBHL emission of 1 kR or less can be produced by a much smaller energy flux of a large bin case (Figure 6b) than of a small bin case as shown in Figure 6a. Hence while the relationship between the energy flux and the LBHL irradiance shows a linear property in global imaging [*Brittnacher et al.*, 1997], the present study shows that it strongly depends on the selection of the bin size or the spatial scale. In the case of small bin size, higher-energy flux produces a more

intense LBHL irradiance, for which the relation is close to a quadratic ($P \sim 0.6$).

5. Summary and Conclusion

[24] FUV spectral observations of aurora arcs were compared with precipitating electrons that were measured simultaneously on the same spacecraft. The kilometer-scale FUV aurora was resolved and it was validated that the FUV auroral irradiance correlates well with total energy flux from 100 eV to 20 keV precipitating electrons measured by ESA. Emissions were accumulated along the line of sight within the vicinity of the footprint that corresponded to a 10 km spatial width at 100 km height. A precise comparison between the FUV aurora and ESA electron spectra was performed, which overcame the previous difficulty of matching the work of the auroral intensity with the particle information.

[25] Selected inverted-V events were classified with peak energy bins at ~1 keV, 3–5 keV, 7–10 keV, and >10 keV. The line spectra from this sorting gave a significant energy dependence on the ratio of LBHL over LBHS, which is known as a good diagnostic indicator for auroral electron precipitation. Comparison with modeling shows a similar trend of LBHL increasing along the peak energy.

[26] Analysis of the downward electron energy flux with the LBHL irradiance shows a strong correlation between the inverted-V structure events especially for peak energy >2 keV with a correlation coefficient of 0.96. Noticeable is that the exponent value of the simple power law is ~0.6, which is different from the linear relation previously obtained between the electron energy flux and the LBHL emission. The difference comes from the selected bin size of the image (~10 km × 10 km or 70 km × 140 km) indicating that the LBHL intensity with precipitating electron energy flux must be interpreted based on imaging bin size dependence.

[27] **Acknowledgments.** FIMS/SPEAR is a joint space project of KAIST and KASI in Korea and U.C. Berkeley and NASA in the United States. One of coauthors (K.-H. Kim) was supported by WCU program through NRF funded by MEST of Korea (R31-10016).

[28] Robert Lysak thanks Takeshi Sakanoi and James Spann for their assistance in evaluating this paper.

References

Ajello, J. M., and D. E. Shemansky (1985), A reexamination of important cross sections by electron impact with application to the dayglow: The Lyman-Birge-Hopfield band system and N I (119.99 nm), *J. Geophys. Res.*, *90*, 9845.

Brittnacher, M., R. Elsen, G. Parks, L. Chen, G. Germany, and J. Spann (1997), A dayside auroral energy deposition case study using the Polar Ultraviolet Imager, *Geophys. Res. Lett.*, *24*, 991.

Carbary, J. F., T. Sotirelis, P. T. Newell, and C.-I. Meng (2004), Correlation of LBH intensities with precipitating particle energies, *Geophys. Res. Lett.*, *31*, L13801, doi:10.1029/2004GL019888.

Carver, J. H., L. A. Davis, B. H. Horton, and M. Ilyas (1978), Ultraviolet extinction measurements of molecular oxygen density, *J. Geophys. Res.*, *83*, 4377.

Coumans, V., J.-C. Gérard, B. Hubert, and D. S. Evans (2002), Electron and proton excitation of the FUV aurora: Simultaneous IMAGE and NOAA observations, *J. Geophys. Res.*, *107*(A11), 1347, doi:10.1029/2001JA009233.

Edelstein, J., et al. (2006a), The "Spectroscopy of Plasma Evolution From Astrophysical Radiation" mission, *Astrophys. J.*, *644*, L153–L158.

Edelstein, J., et al. (2006b), The Spear instrument and on-orbit performance, *Astrophys. J.*, *644*, L159–L162.

Frey, H. U., S. B. Mende, C. W. Carlson, J.-C. Gérard, B. Hubert, J. Spann, R. Gladstone, and T. J. Immel (2001), The electron and proton aurora as seen by IMAGE-FUV and FAST, *Geophys. Res. Lett.*, *28*, 1135.

Frey, H. U., S. B. Mende, T. J. Immel, J.-C. Gérard, B. Hubert, S. Habraken, J. Spann, G. R. Gladstone, D. V. Bisikalo, and V. I. Shematovich (2003), Summary of quantitative interpretation of IMAGE far ultraviolet auroral data, *Space Sci. Rev.*, *109*, 255.

Gérard, J.-C., B. Hubert, M. Meurant, V. I. Shematovich, D. V. Bisikalo, H. Frey, S. Mende, G. R. Gladstone, and C. W. Carlson (2001), Observation of the proton aurora with IMAGE FUV imager and simultaneous ion flux in situ measurements, *J. Geophys. Res.*, *106*, 28,939.

Germany, G. A., M. R. Torr, P. G. Richards, and D. G. Torr (1990), The dependence of modeled OI 1356 and N_2 Lyman Birge Hopfield auroral emissions on the neutral atmosphere, *J. Geophys. Res.*, *95*, 7725.

Germany, G. A., M. R. Torr, D. G. Torr, and P. G. Richards (1994), Use of FUV auroral emissions as diagnostic indicators, *J. Geophys. Res.*, *99*, 383.

Germany, G. A., G. K. Parks, M. Brittnacher, J. Cumnock, D. Lummerzheim, J. F. Spann, L. Chen, P. G. Richards, and F. J. Rich (1997), Remote determination of auroral energy characteristics during substorm activity, *Geophys. Res. Lett.*, *24*, 995.

Germany, G. A., D. Lummerzheim, and P. G. Richards (2001), Impact of model differences on quantitative analysis of FUV auroral emissions: Total ionization cross sections, *J. Geophys. Res.*, *106*, 12,837.

Hedin, A. E. (1991), Extension of the MSIS thermosphere model into the middle and lower atmosphere, *J. Geophys. Res.*, *98*, 1159.

Kunitake, M., and T. Oguti (1984), Spatial-temporal characteristics of flickering spots in flickering auroras, *J. Geomagn. Geoelectr.*, *36*, 121.

Lee, J.-J., et al. (2005), Energy spectra of 170–360 keV electron microbursts measured by the Korean STSAT-1, *Geophys. Res. Lett.*, *32*, L13106, doi:10.1029/2005GL022996.

Liou, K., P. T. Newell, C.-I. Meng, and T. Sotireles (1999), Source region of 1500 MLT auroral bright spots: Simultaneous Polar UV-images and DMSP particle data, *J. Geophys. Res.*, *104*, 24,587.

Lummerzheim, D., and J. Lilensten (1994), Electron transport and energy degradation in the ionosphere: Evaluation of the numerical solution, comparison with laboratory experiments and auroral observations, *Ann. Geophys.*, *12*, 1039.

McFadden, J. P., C. W. Carlson, M. H. Boehm, and T. J. Hallinan (1987), Field-aligned electron flux oscillations that produce flickering aurora, *J. Geophys. Res.*, *92*, 11,133.

Mende, S. B., C. W. Carlson, H. U. Frey, T. J. Immel, and J.-C. Gérard (2003), IMAGE FUV and in situ FAST particle observations of substorm aurorae, *J. Geophys. Res.*, *108*(A4), 1145, doi:10.1029/2002JA009413.

Meurant, M., J.-C. Gérard, B. Hubert, V. Coumans, C. Blockx, N. Østgaard, and S. B. Mende (2003), Dynamics of global scale electron and proton precipitation induced by a solar wind pressure pulse, *Geophys. Res. Lett.*, *30*(20), 2032, doi:10.1029/2003GL018017.

Newell, P. T., K. Liou, and C.-I. Meng (1999), Dynamics of double-theta aurora: Polar UVI study of January 10–11, 1997, *J. Geophys. Res.*, *104*, 95.

Paxton, L. J., et al. (1999), Global ultraviolet imager (GUVI): measuring composition and energy inputs for the NASA Thermosphere Ionosphere Mesosphere Energetics and Dynamics (TIMED) mission, *SPIE Opt. Spectrosc. Tech. Instrum. Atmos. Space Res. III*, *3756*, 265–276.

Strickland, D. J., J. R. Jasperse, and J. A. Whalen (1983), Dependence of auroral FUV emissions on the incident electron spectrum and neutral atmosphere, *J. Geophys. Res.*, *88*, 8051.

Torr, M. R., et al. (1995), A far ultraviolet imager for the international solar-terrestrial physics mission, *Space Sci. Rev.*, *71*, 329.

Yoshino, K., W. H. Parkinson, K. Ito, and T. Matsui (2005), Absolute absorption cross-section measurements of Schumann-Runge continuum of O_2 at 90 and 295 K, *J. Mol. Spectrosc.*, *229*, 238.

Zhang, Y., L. J. Paxton, T. J. Immel, H. U. Frey, and S. B. Mende (2003), Sudden solar wind dynamic pressure enhancements and dayside detached auroras: IMAGE and DMSP observaions, *J. Geophys. Res.*, *108*(A4), 8001, doi:10.1029/2002JA009355.

K. S. Cho, W. Han, J.-J. Lee, and Y. D. Park, Korea Astronomy and Space Science Institute, Daejeon, 305-348, Korea.

J. Edelstein, M. O. Fillingim, E. Korpela, and G. K. Parks, Space Sciences Laboratory, University of California, 7 Gauss Way, Berkeley, CA 94720, USA.

K. H. Kim, School of Space Research, Kyung Hee University, Yongin-Si, Gyeonggi-Do, 446-701, Korea.

Y. H. Kim, Astronomy and Space Science, ChungNam National University, Daejeon, 305-764, Korea.

C. N. Lee and K. W. Min, Department of Physics, Korea Advanced Institute of Science and Technology, Daejeon, 305-701, Korea. (cnlee@space.kaist.ac.kr)

D. Lummerzheim, Geophysical Institute, University of Alaska Fairbanks, 505 South Chandalar Drive, Fairbanks, AK 99775, USA.